

See discussions, stats, and author profiles for this publication at: <https://www.researchgate.net/publication/279210102>

Effect of Charge Transfer in Magnetic-Plasmonic Au@MO_x (M = Mn, Fe) Heterodimers on the Kinetics of Nanocrystal Formation

ARTICLE in CHEMISTRY OF MATERIALS · JUNE 2015

Impact Factor: 8.35 · DOI: 10.1021/acs.chemmater.5b01968

READS

86

8 AUTHORS, INCLUDING:



Benjamin Balke

Johannes Gutenberg-Universität Mainz

128 PUBLICATIONS 2,317 CITATIONS

SEE PROFILE



Martin Panthöfer

Johannes Gutenberg-Universität Mainz

94 PUBLICATIONS 801 CITATIONS

SEE PROFILE



Frédéric Laquai

King Abdullah University of Science and Techn...

101 PUBLICATIONS 2,032 CITATIONS

SEE PROFILE



Wolfgang Tremel

Johannes Gutenberg-Universität Mainz

557 PUBLICATIONS 7,529 CITATIONS

SEE PROFILE

Effect of Charge Transfer in Magnetic-Plasmonic Au@MO_x (M = Mn, Fe) Heterodimers on the Kinetics of Nanocrystal Formation

Isabel Schick,[†] Dominik Gehrig,[‡] Mirko Montigny,[†] Benjamin Balke,[§] Martin Panthöfer,[†] Andreas Henkel,^{||} Frédéric Laquai,[‡] and Wolfgang Tremel^{*,†}

[†]Institut für Anorganische Chemie und Analytische Chemie, Johannes Gutenberg-Universität, Duesbergweg 10-14, 55128 Mainz, Germany

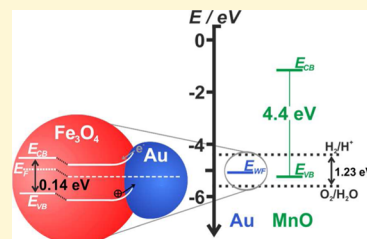
[‡]Max-Planck-Forschungsgruppe für Organische Optoelektronik, Max-Planck-Institut für Polymerforschung, Ackermannweg 10, 55128 Mainz, Germany

[§]Institut für Anorganische Chemie und Analytische Chemie, Johannes Gutenberg-Universität, Staudingerweg 9, 55128 Mainz, Germany

^{||}Zentrum für Datenverarbeitung, Johannes Gutenberg-Universität, Anselm-Franz-von-Bentzel-Weg, 55128 Mainz, Germany

S Supporting Information

ABSTRACT: Heteronanoparticles represent a new class of nanomaterials exhibiting multifunctional and collective properties, which could find applications in medical imaging and therapy, catalysis, photovoltaics, and electronics. This present work demonstrates the intrinsic heteroepitaxial linkage in heterodimer nanoparticles to enable interaction of the individual components across their interface. It revealed distinct differences between Au@MnO and Au@Fe₃O₄ regarding the synthetic procedure and growth kinetics, as well as the properties to be altered by the variation of the electronic structure of the metal oxides. The chemically related metal oxides differ concerning their band gap; while MnO is a Mott-Hubbard insulator with a large band gap, Fe₃O₄ is a semimetal with thermally activated conductivity. The fluorescence dynamics indicate a prolonged relaxation time (>2 ns) for electrons of the conduction band of the Au nanoparticles after interfacing to Fe₃O₄. Here, the semiconduction is not depleted and forms an ohmic contact to the Au domain. In contrast, the fluorescence dynamics and ESCA of Au@MnO affirmed the weak interaction with the electrons of the Au domain, where the junction behaves as a Schottky barrier.



INTRODUCTION

A key aspect of heteronanoparticles is their communication across the solid state interface. The most prominent heteronanostructures are plasmonic photocatalysts, which combine two synergistic features: a Schottky junction enhancing charge separation and the surface plasmon resonance, which is responsible for strong absorption of visible light and the excitation of charge carriers within the photocatalyst. However, the emergence of a Schottky junction is not limited to plasmonic photocatalysts, but rather is an intrinsic feature of heterodimer nanoparticles.¹ To date, there are plenty of examples of interfacial interactions inducing new properties that are not present in the individual components. This is attributed to an electron transfer across the nanometer contact at the interface. Upon direct contact between a metal and a semiconductor metal oxide, electrons tend to diffuse from the Fermi level of the metal to the conduction band of the metal oxide. This results in a downward band bending of the metal oxide, which causes charge accumulation at the interface.² Nowadays, it is most prominently used to enhance catalytic properties. Here, the metal oxide domain acts as a charge reservoir, while the metal domain is the catalytically active component where metal–organic reactions proceed. This enhanced catalytic activity in comparison to the single

component nanoparticles was demonstrated for several systems, such as Au@TiO₂,^{3–6} Ag@TiO₂,⁷ Pt@Fe₃O₄,⁸ Au@ZnO,^{3,9} Ni@Fe₂O₃,¹⁰ Ag@Fe₃O₄,¹¹ and Au@Fe₃O₄.^{12–14} Moreover, an alternation of magnetic or optical properties was observed.^{15–18} Due to the well-defined morphology and the tunability of the domain sizes, heterodimers are an ideal system to analyze not only the properties that are caused by the intrinsic characteristics of the individual components but also the communication between the two components.²

Recently, Au@MnO as well as Au@Fe₃O₄ heterodimer nanoparticles have been investigated for their biomedical application^{19,20} as contrast agents for multimodal imaging^{21–23} as well as highly functional hybrid materials with exceptional control over surface functionalization.^{24–26} At a first glance, Au@MnO and Au@Fe₃O₄ heterodimer nanoparticles share many characteristics, e.g., synthetic methods and optical properties, as well as the tunability of their morphology and domain sizes.^{21,26–28} Irrespective of the chemical composition of the metal oxide domain, the facile control over morphology and domain sizes has been demonstrated and exploited to

Received: May 26, 2015

Revised: June 6, 2015

Published: June 8, 2015

adjust the particles' characteristics. Still, a detailed study revealed pronounced differences in the growth kinetics and morphology control, which can be related to the interfacial communication and the charge transfer. Owing to the strong coupling between the two domains sharing a common interface in heterodimer nanoparticles, the distinct electronic structure of MnO^{29} and $\text{Fe}_3\text{O}_4^{30,31}$ is shown to bias the interfacial communication across the solid state interface and, thus, to control their intrinsic optical characteristics.

EXPERIMENTAL SECTION

Materials. Tetrachloroauric(III) acid hydrate (51% Au, $\text{HAuCl}_4 \cdot (\text{H}_2\text{O})_x$) was purchased from ABCR. Tetralin (1,2,3,4-tetrahydronaphthalene) (anhydrous, 99%), borane *tert*-butylamine complex (TBAB, 97%), 1-octadecane-thiol (ODT, 98%), manganese(II) chloride tetrahydrate ($\text{MnCl}_2 \cdot 4\text{H}_2\text{O}$, Reagent Plus, > 99%), iron(III) chloride hexahydrate ($\text{FeCl}_3 \cdot 6\text{H}_2\text{O}$, Reagent Plus, 98%), sodium oleate (>82% fatty acids (as oleic acid) basis), sodium hydroxide (99%), and 1-octadecene (90%) were purchased from Sigma-Aldrich. Acetone, hexane, methanol, oleic acid (Reagent grade), oleylamine (OAm, 80–90%), and toluene were purchased from Fisher Scientific. All chemicals were used without further purification.

Monodisperse Au nanoparticles were prepared according to Peng et al.³² with some modifications.²⁶ Au@MnO heterodimer nanoparticles were synthesized in a seed-mediated nucleation and growth process by thermal decomposition of manganese(II) oleate³³ on preformed 1-octadecanethiol-functionalized Au, as was reported previously by us.²⁶

Synthesis of $\text{Au@Fe}_3\text{O}_4$ Heterodimer Nanoparticles. The synthetic protocol was developed in analogy to Au@MnO heterodimers based on reports by Lin et al. with modifications concerning the heating program as well as the ligand ratio.³⁴ For 7@20 nm heterodimers, 0.4 mmol of iron(III) oleate³⁵ was dissolved in a mixture composed of 30 mL of 1-octadecene, 8 mmol of oleylamine, and 6 mmol of oleic acid at 80 °C under argon atmosphere. A total of 30 mg of oleylamine-functionalized Au nanoparticles were added in 1 mL of 1-octadecene. In the next step, the reaction mixture was heated to reflux to 320 °C with a heating rate of 2 °C/min. It was held at reflux for 30 min before cooling down to room temperature by removing the heating mantle. The particles were washed twice by precipitation with 2-propanol, centrifugation, and dissolution in hexane.

Nanoparticle Characterization. The particles were characterized by means of (high resolution) transmission electron microscopy ((HR-)TEM), UV-vis, and fluorescence spectroscopy. High resolution TEM images were recorded using a FEI Tecnai F30 S-TWIN instrument with a 300 kV field emission gun and low resolution TEM images using a Philips EM420 microscope with an acceleration voltage of 120 kV. Samples for (HR-)TEM were prepared by dropping a dilute solution of nanoparticles in hexane onto a carbon coated copper grid (Plano, Wetzlar, Germany). UV-vis spectra were collected by a Varian Cary 5000 UV-vis/NIR-spectrometer. Transient emission spectra on a picosecond time scale were taken with a Streak Camera System (Hamamatsu C4742). The excitation wavelength was 400 nm provided by the frequency-doubled output of a Coherent MIRA Ti:sapphire laser system. High resolution synchrotron powder diffraction data were collected at the beamline 11-BM at the Advanced Photon Source (APS), Argonne National Laboratory, using a calibrated average wavelength of 0.413715 Å. Discrete detectors covering an angular range from -6° to 16° 2θ are scanned over a 34° 2θ range, with data points collected every 0.001° 2θ and a scan speed of $0.1^\circ/\text{s}$. The samples were mounted in Kapton tubes with 0.4 mm radii. Rietveld refinements of all diffraction data were performed with TOPAS Academic V5³⁶ applying the fundamental parameter approach. ESCA data for Au@MO_x nanoparticles were measured with an ESCA from PREVAC equipped with an SCIENTA R4000 X-ray photoelectron spectrometer using Al $K\alpha$ radiation (450 W, 15 kV, 30 mA). The binding energy was calibrated by setting the C 1s peak to 284.5 eV. The resolution of the ESCA analysis is ca. 1.0 eV.

RESULTS AND DISCUSSION

Particle Synthesis. Au@MO_x ($M = \text{Mn, Fe}$) heterodimer nanoparticles were prepared following a seed-mediated growth process starting from oleylamine-functionalized Au seeds.^{26,32} A key step was the preparation of monodisperse seeding nanoparticles with distinct size and surface functionalization. For this purpose, separate preparation of seed particles was superior to a one-pot synthesis. However, the surface functionalization of the seeds is crucial, as it has to be compatible with the subsequent growth conditions. Furthermore, the binding strength can control epitaxial overgrowth of metal oxides on noble metal nanoparticles.³⁷ Heterogeneous nucleation of the metal oxide domains on the preformed Au seeds was achieved by thermal decomposition of the metal oleate precursors in 1-octadecene with oleic acid and oleylamine added as ligands. Ligand-capped Ag clusters with electron withdrawing ligands³⁸ and self-assembled monolayers of thiols have been reported to decrease the work function value of bare Ag.³⁹ Similarly, functionalization of the Au nanoparticles with a surface-passivating thiol prior to the nucleation of the metal oxide domain turned out to be crucial to obtain Au@MnO heterodimers independent of the size of the Au seed particles (Supporting Information Figure S1). 1-Octadecane-thiol as ligand was found to suppress multiple nucleation of MnO, which lead to “flowerlike” Au@MnO heteronanoparticles (Figure 1a,b). In contrast, the pristine oleylamine-functionalized Au seeds could be used for the preparation of monodisperse $\text{Au@Fe}_3\text{O}_4$ heterodimer nanoparticles (Figure 1c,d).

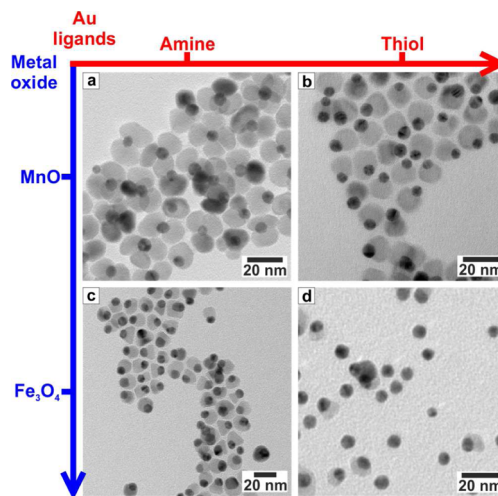


Figure 1. Overview TEM bright field images of Au@MO_x ($M = \text{Mn, Fe}$) heteronanoparticles showing the influence of the functionalization of the preformed Au nanoparticles on the resulting morphology of the heteronanoparticles, which is dependent on the metal oxide: OAm-functionalized Au nanoparticles lead to (a) flower-like Au@MnO but (c) $\text{Au@Fe}_3\text{O}_4$ heterodimers, while ODT-functionalized Au NPs result in (c) Au@MnO heterodimers but (d) little $\text{Au@Fe}_3\text{O}_4$ heteronanoparticles with a large fraction of nonreacted Au NPs.

Independent of the metal oxide, monodisperse heterodimer nanoparticles with tunable domain sizes were obtained. For Au nanoparticles of a given size, the diameter of the metal oxide domains was controlled via the ratio of metal oleate to Au seeds. Further, homogeneous nucleation of metal oxide

nanoparticles was suppressed by lowering the precursor concentration below critical supersaturation conditions.²⁶

The Au nanoparticles were polycrystalline and showed typical 5-fold twinning (Figure 2 a,b,c). Thus, the different

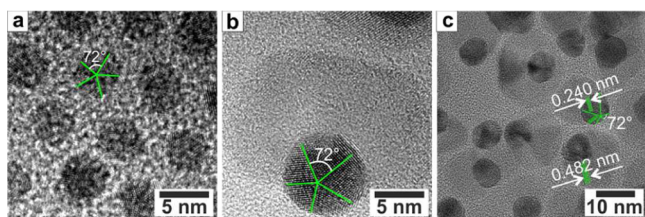


Figure 2. HR-TEM images of (a) Au, (b) Au@MnO, and (c) Au@Fe₃O₄ nanoparticles.

synthetic behavior regarding the formation of anisotropic heterodimer nanoparticles cannot be explained by preferred nucleation on distinct crystal facets, which showed different affinity or binding strength to the ligands. No significant ripening of the Au nanoparticles was observed when being heated to 320 °C in the reaction mixture (Supporting Information Figure S2). HR TEM analysis revealed hetero-epitaxial growth of the metal oxide domains on the Au seeds on the (111) facets (Figure 2c), as was confirmed by the distance between adjacent atomic planes.

The phase composition of the as-prepared heterodimer nanoparticles and Au seeds was investigated by high-resolution synchrotron powder X-ray diffraction. Figure 3 displays typical powder XRD patterns of 5 nm Au, 7@20 nm Au@MnO, and 9@15 nm Au@Fe₃O₄ nanoparticles. The positions and relative intensities are in good accordance with the expected pattern for

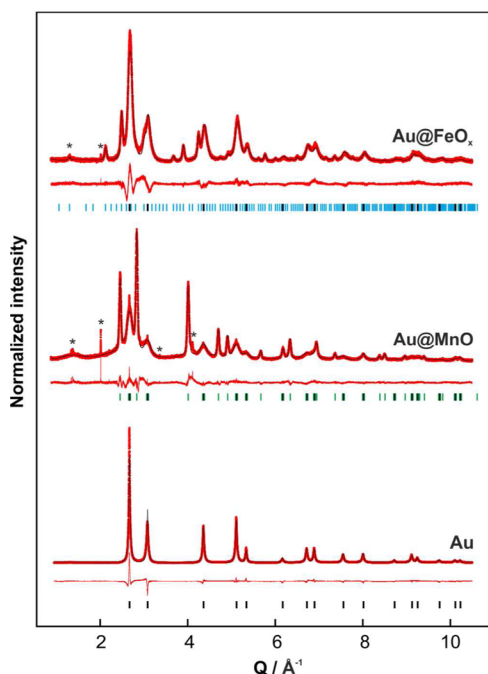


Figure 3. Refined synchrotron powder diffraction data of Au, Au@MnO, and Au@Fe₃O₄ (red dots), including profiles (black solid lines) and profile differences (red solid lines). The refined peak positions are indicated by black (Au), green (MnO), and Fe₃O₄ (blue) tick marks. Contaminations are marked by asterisks.

fcc-type Au, rock-salt-type MnO, and the inverse-spinel-type FeO_x.

The crystallite sizes determined from the reflection profiles coincided with the particle and crystallite sizes observed in TEM analysis (see Supporting Information Table S1). The phase composition of the iron oxide was approximated to Fe_{0.733(9)}O by refinement of the site occupancy, which corresponded to magnetite as the main component. The slightly reduced iron content indicated a minor contamination by Fe₂O₃, which could originate from partial oxidation at the surface.

Growth Mechanism. As an in situ observation of the nucleation by common techniques remains challenging, aliquots of a typical synthesis of Au@MO_x heterodimers were taken to monitor the mechanism. The first aliquots were taken at 260 °C, thus 90 min after the heating ramp was started. According to the heating rate of 2 °C/min, the subsequent 5 min-increment was equal to 10 °C. The reaction snapshots were analyzed without any purification, as the usually applied centrifugation and redissolution procedure could have an influence on the composition. The position as well as the spectral intensity were determined to be directly related to the MO_x domain size.^{26–28} Therefore, UV–vis spectroscopy could be used as a powerful technique to examine the evolution of the heterodimer nanoparticles.

Au@MnO Heterodimers. Within the first 110 min after starting the heating process the absorption intensity decreased slightly (Figure 4a). Starting at 310 °C, after 115 min, the spectral intensity dropped drastically indicating sudden nucleation of the electron deficient material on the Au nanoparticles. During the remaining reaction time of 25 min, the absorption intensity varied only slightly again. Coinciding with the observed drop in intensity, the absorption maximum showed a significant bathochromic shift confirming the sudden heterogeneous nucleation. At first glance, this observation contradicted the nucleation behavior of manganese oleate forming spherical MnO nanoparticles. Schladt et al.¹⁵ reported the decomposition to start already at 215 °C forming poorly crystalline particles. However, upon close examination, this discrepancy could be attributed to the differences concerning the nature of nucleation: the formation of MnO nanoparticles is a homogeneous nucleation, whereas Au@MnO nanoparticles form heterogeneously. As compared to the formation of pure MnO nanoparticles, the concentration of manganese oleate was lowered in order to suppress homogeneous nucleation. Thus, even though the same precursor was used, the reaction kinetics were designed to differ according to the morphology of the nanoparticles.

TEM analysis of the reaction snapshots confirmed the suggestion of sudden nucleation at 310 °C. The temporal evolution is shown in Supporting Information Figure S3. No indication of heterogeneous nucleation was observed up to 300 °C. Here, abrupt nucleation of MnO domains occurred at 310 °C, justifying the drastic decrease in spectral intensity. Further temperature increase and prolonged reaction time at a reflux temperature of 320 °C sharpened the size distribution, but no further nucleation was observed. In conclusion, these findings suggest this synthetic approach to proceed according to the LaMer model⁴⁰ for heterogeneous nucleation. The crucial separation of nucleation and growth was achieved by tailoring the reaction conditions. The narrow size distribution of the obtained nanoparticles was attributed to a single nucleation event at 310 °C, which becomes evident upon analysis of the

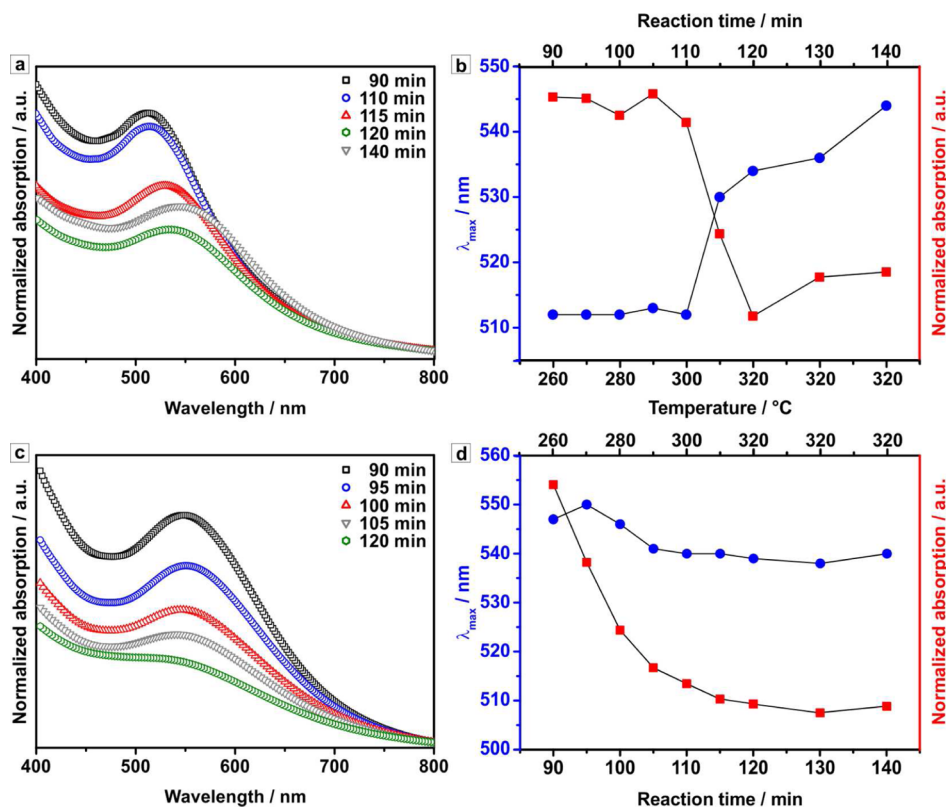


Figure 4. UV–vis spectra of reaction snapshots and corresponding analysis of the UV–vis spectra showing the evolution of the position of the absorption maximum as well as the spectral intensity as a function of reaction time and temperature. The UV–vis spectra were measured without further purification of the aliquots and normalized to 800 nm: (a, b) Au@MnO and (c, d) Au@Fe₃O₄.

UV–vis spectra in terms of evolution of the absorption maximum and the spectral intensity (Figure 4b). Both correlations showed a drastic change upon trespassing 310 °C. This offset represented the sudden change in the local dielectric function of the medium surrounding the gold nanoparticles. Subsequent to the nucleation event, the absorption maximum shifted nearly linear with the reaction time, indicating further growth of the MnO domains. Further, the spectral intensity recovered slightly after the nucleation event. In contrast to the absorption wavelength, the absorption remained constant rather than showing a linear behavior. This indicated that the spectral intensity was insensitive to the proportion of electron deficient material, once conjugation took place.

Au@Fe₃O₄ Heterodimers. In contrast to the sudden change in spectral intensity and absorption wavelength during the growth of Au@MnO heterodimers, the analysis of the aliquots taken during the synthesis of Au@Fe₃O₄ heterodimers showed a continuous decrease in the spectral intensity over time (Figure 4c,d). This red-shift and peak broadening (due to higher order oscillations lower in energy) are associated with a retardation in the heterodimer.⁴¹ The observed trend for the absorption maxima has previously been observed in naked metal nanoparticles,⁴² and it can be explained based on a particle in a box model, where the energy levels are more closely spaced with increasing particle size, which in turn leads to a smaller transition energy of the surface plasmon resonance. This observation corroborated the observation of Kwon et al.,⁴³ who reported the decomposition of the oleate complex to start at 230 °C. As the formation of Au@Fe₃O₄ required only a heterogeneous nucleation step, the energy barrier for Fe₃O₄

was significantly lower. Moreover, the steep slope of spectral intensity as a function of the reaction coordinate suggested a nucleation during the early stages of the reaction. Concurrent with the decline in spectral intensity was a bathochromic shift of the surface plasmon resonance of 517 nm for the Au seeds. The shift was not continuous for the analyzed aliquots, but showed a slight maximum at 270 °C, which may be related to a decomposition of the iron oleate complex to form polyiron oxo clusters.⁴³ These uniformly altered the local dielectric function surrounding the Au seeds. As a consequence, the bathochromic shift was more distinct than for the final anisotropic heterodimers. Accordingly, further growth of the oxide domain did not alter the position of the absorption maximum.

TEM analysis was used to confirm the relationship of nucleation and growth to optical properties. Representative images of the evolution of heterodimer nanoparticles are shown in Supporting Information Figure S4. As suggested by UV–vis spectroscopy, nucleation occurred below 320 °C (approximately 270 °C). However, no burst of nucleation was observed, as nucleation did not proceed simultaneously on all Au. Further increasing the reaction temperature led to heterogeneous nucleation on all Au seeds.

Technically speaking, this nucleation cannot be described in terms of the LaMer model,⁴⁰ as neither a burst of nucleation nor the separation of nucleation and growth could be detected. As was discussed before,⁴³ the homogeneous formation of Fe₃O₄ nanoparticles can be subdivided into two steps: (i) the thermal decomposition of the oleate complex and (ii) the nucleation and growth of the nanoparticles. The homogeneous nucleation was complete after 2 min at 320 °C. Subsequently, a narrowing of the size distribution occurred, before an incipient

defocusing through Ostwald ripening.⁴³ Due to the presence of Au seeds in the reaction mixture, the energy of intermediate species required for nucleation was significantly lowered. Therefore, the nucleation started at lower temperatures than for homogeneous nucleation, but continued until the final temperature of the heating ramp. However, monodisperse Au@Fe₃O₄ heterodimer nanoparticles were obtained after refluxing for 20 min at 320 °C. This can be viewed as a kinetically driven size-focusing effect.⁴⁴

Optical Characteristics. The analysis of the surface plasmon resonance showed a broadening accompanied by a decrease in the spectral intensity compared to Au nanoparticles. Figure 5 displays a direct comparison of the UV–vis spectra.

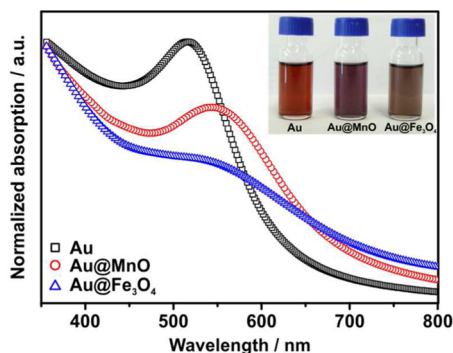


Figure 5. UV–vis spectra of Au, Au@MnO, and Au@Fe₃O₄ nanoparticles revealing the decrease in intensity to be dependent on the composition of the heterodimer nanoparticles. The spectra were measured in *n*-heptane and normalized to 350 nm. Inset: digital image of the nanoparticle solutions.

The difference in spectral intensity is substantial, where Au@MnO displayed intermediate behavior in between that Au and Au@Fe₃O₄. BEM simulations⁴⁵ using the mean sizes as measured by TEM and reported dielectric functions^{46–48} show a similar behavior, i.e. a strong damping and red-shift of the plasmon peak, hence supporting the intrinsic nature of the spectral changes due to the presence of a semiconductor or insulator (Supporting Information Figure S5). The damping of the plasmon is stronger in Au@Fe₃O₄ whereas for Au@MnO the plasmon is still pronounced which hints toward a difference in interfacial communication as reported in the chapter below. The differences were clearly visible after the synthesis as indicated by the colors of the colloidal solutions (Figure 5, inset). Their brilliance decreased upon heterodimer formation. The color of Au@MnO heterodimers as a function of the domain sizes was purple, the solutions of Au@Fe₃O₄ were brownish, and their color showed only a minor size dependence.

Interfacial Communication. The change of the surface plasmon resonance of Au nanoparticles as a result of the chemical composition of the metal oxide domains indicates the communication across the metal–metal oxide Schottky barrier to be strongly dependent on the electronic structure of the two components. Magnetite is known to be a semimetal with a small direct band gap of $\Delta E_{\text{direct}} = 0.14$ eV.^{30,49} In contrast, manganosite is a wide band gap semiconductor with an indirect band gap of $\Delta E_{\text{indirect}} = 3.40$ eV, while it is an insulator concerning its direct band gap of $\Delta E_{\text{direct}} = 4.44$ eV.⁴⁸ As a result, the communication with the Au domains across the interface is fundamentally different. The electronic structure of the Au domains and the heterodimer nanoparticles was

qualitatively characterized by electron spectroscopy for chemical analysis (ESCA). Figure 6a shows the O 1s electron

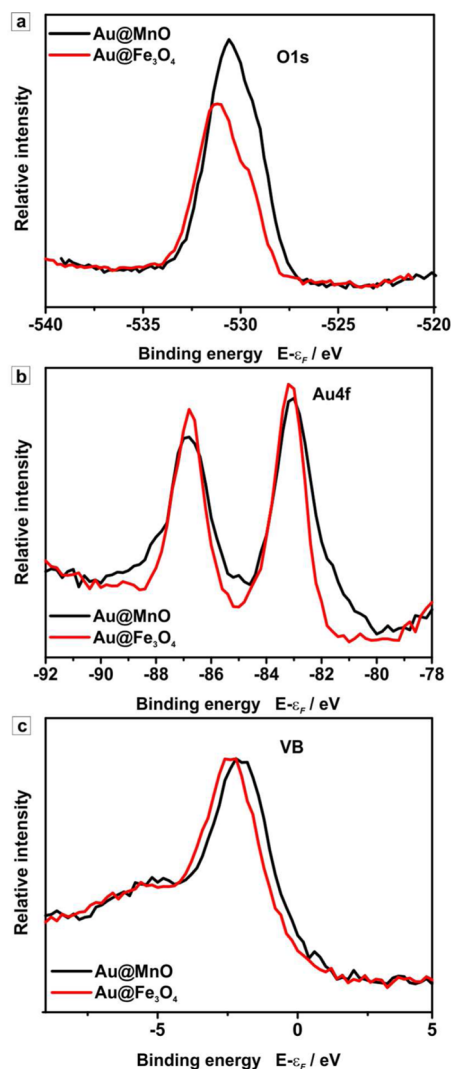


Figure 6. ESCA spectra of Au@MO_x nanoparticles (a) O 1s spectra, (b) Au 4f spectra, and (c) valence band spectra.

binding energy for Au@MnO and Au@Fe₃O₄, where Au@Fe₃O₄ heterodimer nanoparticles display an increase in binding energy of approximately 0.6 eV. An analysis of Au 4f binding energy shows significantly narrower peaks for Au@Fe₃O₄ nanoparticles (Figure 6b). Furthermore, the position of the valence band of Au@Fe₃O₄ is lowered by 0.4 eV as compared to that of Au@MnO heterodimer nanoparticles (Figure 6c). As the reference level (all spectra are calibrated to the C 1s binding energy) did not change, the change in binding energy is attributed to the charge transfer between the Au and Fe₃O₄ domains as previously reported by Pt–Fe₃O₄ nanoparticles.⁸

At the Au/Fe₃O₄ interface the surface states associated with the conduction bands, valence bands, and Fermi level equilibrate due to the electron transfer between the two domains (Figure 7). Therefore, the electron density of the Au nanoparticles decreases, which is directly reflected by the inhibition of multinucleation of Fe₃O₄ on Au seeds (vide supra). When Fe₃O₄ particles nucleate on Au seeds, they become electron deficient due to the charge transfer at the interface and further nucleation is blocked.²⁷

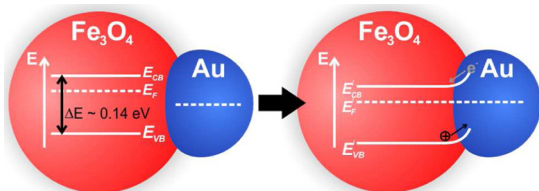


Figure 7. Schottky barrier formed at the Au/Fe₃O₄ metal/semimetal junction.

In contrast, no charge equilibration occurred upon direct contact of Mott–Hubbard insulating MnO²⁹ and Au because of the large band gap. No charge transfer occurs in the case of Au@MnO, and the Au domains retain sufficient electron density to allow multinucleation. Therefore, a surface-passivating thiol is needed in order to synthesize Au@MnO heterodimer nanoparticles.

Excited State Dynamics. These differences in charge transfer across the solid state interface confirm the suggested correlation between the optical properties of Au@MO_x and two parameters: (i) the variation of the local dielectric function, which was common between Au@MnO and Au@Fe₃O₄, and (ii) the so-called “interface decay channel”²⁸ responsible for the electron transfer, which did not take place for Au@MnO. The bathochromic shift of the SPR can be rationalized based on classical Mie theory approximating the changes of the local dielectric environment as a combination of the solvent and MO_x. As the damping remains undeclared by means of Mie’s theory, though it was less pronounced for Au@MnO, a charge transfer effect from Au to MO_x domains is suggested, which results in a modified relaxation behavior as discussed by Wei and co-workers.²⁸

As UV–vis spectroscopy enabled only statements regarding the steady-state behavior, time-resolved photoluminescence spectroscopy (TR-PL) was applied to study the relaxation behavior. The fluorescence spectra and decay dynamics of the pristine Au nanoparticles in comparison to Au@Fe₃O₄ and Au@MnO heterodimers were systematically investigated. The nanoparticles were dissolved in toluene, excited by a femto-second laser pulse at 400 nm, and the subsequent emission was detected by a Streak Camera setup. The time-integrated fluorescence spectra (Figure 8a) showed a close resemblance between thiol-functionalized Au nanoparticles and Au@Fe₃O₄ heterodimers, which had a maximum of photoluminescence at 481 and 475 nm, respectively, and it was shifted to 463 nm for Au@MnO. These heterodimers, however, displayed an additional peak at 632 nm. The emission spectrum of the thiol-functionalized Au nanoparticles is almost congruent with the one of Au@Fe₃O₄ heterodimers, which indicates the Au domains to be the origin of the fluorescence and barely any effect of their ligand exchange.

CONCLUSIONS

This work demonstrates the intrinsic heteroepitaxial junction in heterodimer nanoparticles to enable interaction of the individual components across their interface. It revealed pronounced differences between Au@MnO and Au@Fe₃O₄ regarding the synthetic procedure as well as the properties arising from the electronic structure of the metal oxide components. The reaction kinetics differed with respect to the composition of the nanoparticles. A decreasing electron density of the Au nanoparticles through electron withdrawing

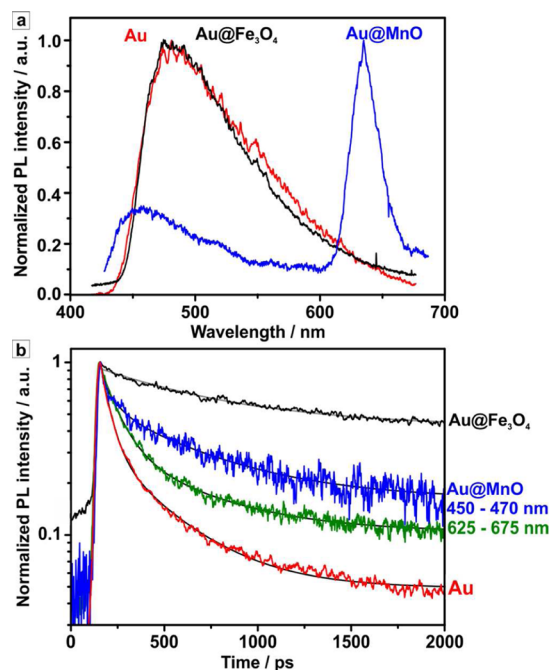


Figure 8. (a) Time-integrated emission spectra of pure Au nanoparticles as well as Au@Fe₃O₄ and Au@MnO heterodimers. The samples were excited at 400 nm by a 100 fs laser pulse. (b) Photoluminescence dynamics monitored at the emission peak wavelength and stretched-exponential fits using the parameter displayed in Table 1.

Table 1. Inverse Decay Rates τ and Stretching Exponent β Obtained from Fitting the Fluorescence Dynamics to a Stretched-Exponential Decay

sample	λ_{em}	τ (ps)	β (s)
Au	480–500 nm	72	0.55
Au@MnO	625–645 nm	107	0.55 (fixed)
Au@MnO	450–470 nm	127	0.55 (fixed)
Au@Fe ₃ O ₄	480–500 nm	2454	0.55 (fixed)

thiol ligands manifests itself by the inhibition of multinucleation of MnO on the Au seeds. In contrast, electron donating amine ligands reverse the reactivity trend and Au@Fe₃O₄ heterodimers are formed. These pronounced differences in the reactivity can be rationalized from the electronic structure of the metal and the metal oxide domains: while MnO is a Mott–Hubbard insulator with a large band gap, Fe₃O₄ is a semimetal with thermally activated (hopping) conductivity. Therefore, the Schottky barrier height Φ_B in Au@MnO is large and significantly higher than the thermal energy kT . As a result, the junction behaves as a Schottky barrier.

In contrast, Au@Fe₃O₄ has lower Schottky barrier height: now the semiconductor is not depleted and forms an ohmic contact to the metal instead. An analysis of the fluorescence dynamics suggests a prolonged relaxation time for the electrons of the conduction band of the Au nanoparticles after interfacing to Fe₃O₄. The fluorescence lifetime for the Au@Fe₃O₄ heteroparticles increased significantly as compared to $\tau < 100$ ps for Au metal nanoparticles. The fluorescence dynamics of Au@MnO affirmed the weak interaction with the electrons of the Au domain. In conclusion, our findings enhance the understanding of the formation of heterodimer nanoparticles

and allow relating the modulated characteristics to the elementary concept of solid state interfaces.

■ ASSOCIATED CONTENT

■ Supporting Information

Details of the measurement and refinement of the high-resolution synchrotron powder X-ray diffraction data (Table S1); TEM images of Au@MnO with tunable domain sizes (Figure S1) and of Au seed particles in comparison to resulting Au@MO_x heterodimers (Figure S2); TEM images of reaction snapshots of typical Au@MnO (Figure S3) and Au@Fe₃O₄ (Figure S4) syntheses; calculated UV-vis spectra from BEM simulations (Figure S5). The Supporting Information is available free of charge on the ACS Publications website at DOI: 10.1021/acs.chemmater.5b01968.

■ AUTHOR INFORMATION

Corresponding Author

*E-mail: tremel@uni-mainz.de.

Author Contributions

All authors have given approval to the final version of the manuscript.

Notes

The authors declare no competing financial interest.

■ ACKNOWLEDGMENTS

This research was supported by the Deutsche Forschungsgesellschaft through the Priority Program 1313 "Bionanoresponses". F.L. thanks the Max Planck Society for funding a Max Planck Research Group. I.S. acknowledges a "Fonds der Chemischen Industrie VCI"-scholarship and is a recipient of a fellowship through the Excellence Initiative (DFG/GSC 266). D.G. is recipient of a Kekulé-scholarship of the "Fonds der Chemischen Industrie". The facilities of the Electron Microscopy Center in Mainz (EZMZ) were supported by the State Excellence Cluster COMATT and SFB 625. We are grateful to the 11-BM beamline staff for their input and technical support. Use of the Advanced Photon Source at Argonne National Laboratory was supported by the U.S. Department of Energy, Office of Science, Office of Basic Energy Sciences, under Contract No. DE-AC02-06CH11357.

■ REFERENCES

- (1) Zhang, X.; Chen, Y. L.; Liu, R.-S.; Tsai, D. P. Plasmonic Photocatalysis. *Rep. Prog. Phys.* **2013**, *76*, 46401.
- (2) Wang, C.; Xu, C.; Zeng, H.; Sun, S. Recent Progress in Syntheses and Applications of Dumbbell-like Nanoparticles. *Adv. Mater.* **2009**, *21*, 3045–3052.
- (3) Kochuveedu, S. T.; Jang, Y. H.; Kim, D. H. A study on the mechanism for the interaction of light with noble metal-metal oxide semiconductor nanostructures for various photophysical applications. *Chem. Soc. Rev.* **2013**, *42*, 8467–8493.
- (4) Subramanian, V.; Wolf, E. E.; Kamat, P. V. Catalysis with TiO₂/Gold Nanocomposites. Effect of Metal Particle Size on the Fermi Level Equilibration. *J. Am. Chem. Soc.* **2004**, *126*, 4943–4950.
- (5) Chen, Y.-S.; Choi, H.; Kamat, P. V. Metal-Cluster-Sensitized Solar Cells. A New Class of Thiolated Gold Sensitizers Delivering Efficiency Greater Than 2%. *J. Am. Chem. Soc.* **2013**, *135*, 8822–8825.
- (6) Jang, Y. H.; Jang, Y. J.; Kochuveedu, S. T.; Byun, M.; Lin, Z.; Kim, D. H. Plasmonic dye-sensitized solar cells incorporated with Au–TiO₂ nanostructures with tailored configurations. *Nanoscale* **2014**, *6*, 1823–1832.

- (7) Hirakawa, T.; Kamat, P. V. Charge Separation and Catalytic Activity of Ag@TiO₂ Core–Shell Composite Clusters under UV–Irradiation. *J. Am. Chem. Soc.* **2005**, *127*, 3928–3934.
- (8) Wang, C.; Daimon, H.; Sun, S.; Dumbbell-like Pt–Fe₃O₄ Nanoparticles. and Their Enhanced Catalysis for Oxygen Reduction Reaction. *Nano Lett.* **2009**, *9*, 1493–1496.
- (9) Li, P.; Wei, Z.; Wu, T.; Peng, Q.; Li, Y. Au–ZnO Hybrid Nanopyramids and Their Photocatalytic Properties. *J. Am. Chem. Soc.* **2011**, *133*, 5660–5663.
- (10) Nakhjavan, B.; Tahir, M. N.; Natalio, F.; Panthöfer, M.; Gao, H.; Dietzsch, M.; Andre, R.; Gasi, T.; Ksenofontov, V.; Branscheid, R.; Kolb, U.; Tremel, W. Ni@Fe₂O₃ heterodimers: controlled synthesis and magnetically recyclable catalytic application for dehalogenation reactions. *Nanoscale* **2012**, *4*, 4571–4577.
- (11) Lopes, G.; Vargas, J. M.; Sharma, S. K.; Béron, F.; Pirota, K. R.; Knobel, M.; Rettori, C.; Zysler, R. D. Ag–Fe₃O₄ Dimer Colloidal Nanoparticles: Synthesis and Enhancement of Magnetic Properties. *J. Phys. Chem. C* **2010**, *114*, 10148–10152.
- (12) Wu, B.; Zhang, H.; Chen, C.; Lin, S.; Zheng, N. Interfacial activation of catalytically inert Au (6.7 nm)-Fe₃O₄ dumbbell nanoparticles for CO oxidation. *Nano Res.* **2009**, *2*, 975–983.
- (13) Lin, F.-h.; Doong, R.-a. Bifunctional Au–Fe₃O₄ Heterostructures for Magnetically Recyclable Catalysis of Nitrophenol Reduction. *J. Phys. Chem. C* **2011**, *115*, 6591–6598.
- (14) Lee, Y.; Garcia, M. A.; Frey Huls, N. A.; Sun, S. Synthetic Tuning of the Catalytic Properties of Au–Fe₃O₄ Nanoparticles. *Angew. Chem., Int. Ed.* **2010**, *49*, 1271–1274.
- (15) Schladt, T. D.; Graf, T.; Köhler, O.; Bauer, H.; Dietzsch, M.; Mertins, J.; Branscheid, R.; Kolb, U.; Tremel, W. Synthesis and Magnetic Properties of FePt@MnO Nano-heteroparticles. *Chem. Mater.* **2012**, *24*, 525–535.
- (16) Sun, X.; Frey Huls, N.; Sigdel, A.; Sun, S. Tuning Exchange Bias in Core/Shell FeO/Fe₃O₄ Nanoparticles. *Nano Lett.* **2012**, *12*, 246–251.
- (17) Furube, A.; Du, L.; Hara, K.; Katoh, R.; Tachiya, M. Ultrafast Plasmon-Induced Electron Transfer from Gold Nanodots into TiO₂ Nanoparticles. *J. Am. Chem. Soc.* **2007**, *129*, 14852–14853.
- (18) Xu, Z.; Hou, Y.; Sun, S. Magnetic Core/Shell Fe₃O₄/Au and Fe₃O₄/Au/Ag Nanoparticles with Tunable Plasmonic Properties. *J. Am. Chem. Soc.* **2007**, *129*, 8698–8699.
- (19) Hoskins, C.; Min, Y.; Gueorguieva, M.; McDougall, C.; Volovick, A.; Prentice, P.; Wang, Z.; Melzer, A.; Cuschieri, A.; Wang, L. Hybrid gold-iron oxide nanoparticles as a multifunctional platform for biomedical application. *J. Nanobiotechnol.* **2012**, *10*, 27.
- (20) Landgraf, L.; Ernst, P.; Schick, I.; Köhler, O.; Oehring, H.; Tremel, W.; Hilger, I. Anti-oxidative effects and harmlessness of asymmetric Au@Fe₃O₄ Janus particles on human blood cells. *Biomaterials* **2014**, *35*, 6986–6997.
- (21) Schladt, T. D.; Shukoor, M. I.; Schneider, K.; Tahir, M. N.; Natalio, F.; Ament, I.; Becker, J.; Jochum, F. D.; Weber, S.; Köhler, O.; Theato, P.; Schreiber, L. M.; Sönnichsen, C.; Schröder, H. C.; Müller, W. E. G.; Tremel, W. Au@MnO nanoflowers: hybrid nanocomposites for selective dual functionalization and imaging. *Angew. Chem., Int. Ed.* **2010**, *49*, 3976–3980.
- (22) Cai, H.; Li, K.; Shen, M.; Wen, S.; Luo, Y.; Peng, C.; Zhang, G.; Shi, X. Facile assembly of Fe₃O₄@Au nanocomposite particles for dual mode magnetic resonance and computed tomography imaging applications. *J. Mater. Chem.* **2012**, *22*, 15110–15120.
- (23) Zhu, J.; Lu, Y.; Li, Y.; Jiang, J.; Cheng, L.; Liu, Z.; Guo, L.; Pan, Y.; Gu, H. Synthesis of Au–Fe₃O₄ heterostructured nanoparticles for in vivo computed tomography and magnetic resonance dual model imaging. *Nanoscale* **2014**, *6*, 199–202.
- (24) Xu, C.; Xie, J.; Ho, D.; Wang, C.; Kohler, N.; Walsh, E. G.; Morgan, J. R.; Chin, Y. E.; Sun, S. Au–Fe₃O₄ Dumbbell Nanoparticles as Dual-Functional Probes. *Angew. Chem., Int. Ed.* **2008**, *47*, 173–176.
- (25) Xu, C.; Wang, B.; Sun, S. Dumbbell-like Au–Fe₃O₄ nanoparticles for target-specific platinum delivery. *J. Am. Chem. Soc.* **2009**, *131*, 4216–4217.

- (26) Schick, I.; Lorenz, S.; Gehrig, D.; Schilmann, A.-M.; Bauer, H.; Panthöfer, M.; Fischer, K.; Strand, D.; Laquai, F.; Tremel, W. Multifunctional Two-Photon Active Silica-Coated Au@MnO Janus Particles for Selective Dual Functionalization and Imaging. *J. Am. Chem. Soc.* **2014**, *136*, 2473–2483.
- (27) Yu, H.; Chen, M.; Rice, P. M.; Wang, S. X.; White, R. L.; Sun, S. Dumbbell-like Bifunctional Au–Fe₃O₄ Nanoparticles. *Nano Lett.* **2005**, *5*, 379–382.
- (28) Wei, Y.; Klajn, R.; Pinchuk, A. O.; Grzybowski, B. A. Synthesis, Shape Control, and Optical Properties of Hybrid Au/Fe₃O₄ “Nanoflowers”. *Small* **2008**, *4*, 1635–1639.
- (29) Anderson, P. W. Local moments and localized states. *Rev. Mod. Phys.* **1978**, *50*, 191–201.
- (30) Goodenough, J. B. Metallic Oxides. *Prog. Solid State Chem.* **1971**, *5*, 145–399.
- (31) Huang, D. J.; Lin, H.-J.; Okamoto, J.; Chao, K. S.; Jeng, H.-T.; Guo, G. Y.; Hsu, C.-H.; Huang, C.-M.; Ling, D. C.; Wu, W. B.; Yang, C. S.; Chen, C. T. Charge-Orbital Ordering and Verwey Transition in Magnetite Measured by Resonant Soft X-Ray Scattering. *Phys. Rev. Lett.* **2006**, *96*, 096401.
- (32) Peng, S.; Lee, Y.; Wang, C.; Yin, H.; Dai, S.; Sun, S. A Facile Synthesis of Monodisperse Au Nanoparticles and Their Catalysis of CO Oxidation. *Nano Res.* **2008**, *1*, 229–234.
- (33) Schladt, T. D.; Graf, T.; Tremel, W. Synthesis and Characterization of Monodisperse Manganese Oxide Nanoparticles—Evaluation of the Nucleation and Growth Mechanism. *Chem. Mater.* **2009**, *21*, 3183–3190.
- (34) Lin, F.-h.; Chen, W.; Liao, Y.-H.; Doong, R.-a.; Li, Y. Effective approach for the synthesis of monodisperse magnetic nanocrystals and M-Fe₃O₄ (M = Ag, Au, Pt, Pd). *Nano Res.* **2011**, *4*, 1223–1232.
- (35) Park, J.; An, K.; Hwang, Y.; Park, J.-G.; Noh, H.-J.; Kim, J.-Y.; Park, J.-H.; Hwang, N.-M.; Hyeon, T. Ultra-large-scale syntheses of monodisperse nanocrystals. *Nat. Mater.* **2004**, *3*, 891–895.
- (36) Coelho, A. *TOPAS Academic V5*; Coelho Software: Brisbane, Australia, 2007.
- (37) Zhang, L.; Dou, Y.-H.; Gu, H.-C. Synthesis of Ag-Fe₃O₄ heterodimeric nanoparticles. *Colloid Interface Sci.* **2006**, *297*, 660–664.
- (38) Dadlani, A. L.; Schindler, P.; Logar, M.; Walch, S. P.; Prinz, F. B. Energy States of Ligand Capped Ag Nanoparticles: Relating Surface Plasmon Resonance to Work Function. *J. Phys. Chem. C* **2014**, *118*, 24827–24832.
- (39) Rusu, P.; Brocks, G. Energy States of Ligand Capped Ag Nanoparticles: Relating Surface Plasmon Resonance to Work Function. *Phys. Rev. B* **2006**, *74*, 73414/1–4.
- (40) LaMer, V.; Dinegar, R. H. Theory, Production and Mechanism of Formation of Monodispersed Hydrosols. *J. Am. Chem. Soc.* **1950**, *72*, 4847–4854.
- (41) Ghosh, S. K.; Pal, T. Interparticle Coupling Effect on the Surface Plasmon Resonance of Gold Nanoparticles: From Theory to Applications. *Chem. Rev.* **2007**, *107*, 4797–4862.
- (42) Liebsch, A. Surface-plasmon dispersion and size dependence of Mie resonance: Silver versus simple metals. *Phys. Rev. B* **1993**, *48*, 11317–11328.
- (43) Kwon, S. G.; Piao, Y.; Park, J.; Angappane, S.; Jo, Y.; Hwang, N.-M.; Park, J.-G.; Hyeon, T. Kinetics of Monodisperse Iron Oxide Nanocrystal Formation by “Heating-Up” Process. *J. Am. Chem. Soc.* **2007**, *129*, 12571–12584.
- (44) Peng, X.; Wickham, J.; Alivisatos, A. P. Kinetics of II-VI and III-V Colloidal Semiconductor Nanocrystal Growth: “Focusing” of Size Distributions. *J. Am. Chem. Soc.* **1998**, *120*, 5343–5344.
- (45) Hohenester, U.; Trügler, A. MNPBEM – A Matlab toolbox for the simulation of plasmonic nanoparticles. *Comput. Phys. Commun.* **2012**, *183*, 370–381.
- (46) Johnson, P. B.; Christy, R. W. Optical Constants of the Noble Metals. *Phys. Rev. B* **1972**, *6*, 4370–4379.
- (47) Schlegel, A.; Alvarado, S. F.; Wachter, P. Optical properties of magnetite (Fe₃O₄). *J. Phys. C: Solid State Phys.* **1979**, *12*, 1157–1164.
- (48) Park, J.-W.; Kim, S.; Choi, S.-H.; Lee, H. Optical Properties of Transition-metal Oxides of MnO and Fe_{0.925}O Crystals Studied with Spectroscopic Ellipsometry and Raman Spectroscopy. *New Physics* **2013**, *63*, 818–825.
- (49) Cabot, A.; Puentes, V. F.; Shevchenko, E.; Yin, Y.; Balcells, L.; Marcus, M. A.; Hughes, S. M.; Alivisatos, A. P. Vacancy Coalescence during Oxidation of Iron Nanoparticles. *J. Am. Chem. Soc.* **2007**, *129*, 10358–10360.